# Efficient Segmentation and Classification of Leukemia Cells via Optimized Deep Graph Attention Network

S. Vijayanand1*
1*Department of Electronics and Communication Engineering, Sri Venkateswara College of Engineering, Sriperumbudur, Chennai 602117, India.
vijayanands185@gmail.com

Ayub Khan. A3
3Assistant Professor, Department of Electronics and Communication Engineering, Sona College of Technology, Salem, Tamil Nadu,India
yubkhan567@outlook.com

P. Divyabharathi2
2Placement Trainer, Department of Electronics and Communication Engineering, Veltech Rangarajan Dr. Sagunthala R&D Institute of Science and Technology, Chennai, Tamil Nadu, India
pdivyabharathi400@outlook.com

R. Giri Prasad4
4Associate Professor, Department of Petroleum Technology. Aditya University, Surampalem, Andhra Pradesh, India
giri.456prasad@gmail.com

***Abstract*— Leukemia is a cancer affecting blood-forming tissues, leading to an abnormal increase in white blood cells (WBCs), making early and accurate diagnosis essential for improving treatment outcomes and patient prognosis. Traditional diagnostic methods such as microscopic examination of blood smears are time-consuming, subjective, and reliant on expert interpretation. Similarly, conventional machine learning techniques struggle with misclassification, low detection rates, and high computational costs. To address these challenges, this study proposes a novel and efficient deep learning-based classification framework for leukemia detection. The approach begins with the collection of input images from publicly available datasets, which are pre-processed using the Pre-Gaussian Discrete Wavelet Transformer (PGDWT) to enhance image quality. Segmentation of the cancerous regions is performed using the Anatomy-Aware Hover Transformer (AAHT), followed by feature extraction. Classification is then executed using a deep Similarity-Navigated Graph Diffusion Kernel Attention Network (SNGDKANet), specifically designed for precise categorization of various leukemia types. To further improve classification accuracy, the Osprey Optimization Algorithm (OOA) is employed for hyperparameter tuning. The model's performance is rigorously evaluated based on several metrics, including accuracy (99.5%), sensitivity (99.8%), recall (99.4%), specificity (99.7%), F1-score (99.6%), and precision (99.7%), with a reduced error rate of 3% and an execution time of just 7 seconds. This performance is benchmarked using three well-known leukemia datasets: SN-AM, ALL-IDB, and C-NMC 2019. The results affirm that the proposed framework significantly outperforms existing methods, offering a highly reliable, fast, and accurate tool for leukemia diagnosis in clinical and research settings.***

*Index Terms*— ***Leukemia, White Blood Cells (WBCs), Deep Learning (DL), Gaussian Discrete Wavelet Transformer (PGDWT), Anatomy-Aware Hover Transformer (AAHT), Similarity-Navigated Graph Diffusion Kernel Attention Network (SNGDKANet), Osprey Optimization Algorithm (OOA).***

**List of Abbreviations and Abbreviations**

**List of Abbreviations**

| **Abbreviations** | **Explanation** |
|---|---|
| AAHT | Anatomy-Aware Hover Transformer |
| ALL | Acute Lymphoblastic Leukemia |
| ALL-IDB | Acute Lymphoblastic Leukemia - Image Database |
| AML | Acute Myeloid Leukemia |
| AUC | Area Under the Curve |
| B-ALL | B-Lineage Acute Lymphoblastic Leukemia |
| CLL | Chronic Lymphoblastic Leukemia |
| CML | Chronic Myeloid Leukemia |
| CNN | Convolutional Neural Network |
| DKAN | Diffusion Kernel Attention Network |
| DL | Deep Learning |
| DWT | Discrete Wavelet Transform |
| F1-Score | Harmonic Mean of Precision and Recall |
| GCL | Graph Convolution Layer |
| GLCM | Gray Level Co- |

| | |
|---|---|
| | occurrence Matrix |
| MCC | Matthews Correlation Coefficient |
| MLP | Multi-Layer Perceptron |
| MM | Multiple Myeloma |
| MSE | Mean Square Error |
| O-CNN | Optimized Convolutional Neural Network |
| OOA | Osprey Optimization Algorithm |
| PGDWT | Pre-Gaussian Discrete Wavelet Transformer |
| ReLU | Rectified Linear Unit |
| ROI | Region of Interest |
| SN-AM | Sanguinaria and Neutrophil-Aggregate Microscopy |
| SNGDKANet | Similarity-Navigated Graph Diffusion Kernel Attention Network |
| SNGNN | Similarity-Navigated Graph Neural Network |
| SVM | Support Vector Machine |
| TPR | True Positive Rate |
| WBC(s) | White Blood Cell(s) |

**List of Symbols**

| **Symbol** | **Explanation** |
|---|---|
| $q$ and $r$ | pixel distances from the center |
| $\rho$ | smoothing level |
| $f(t)$ | image function |
| $\lambda_{q,r}(t)$ | wavelet basis function |
| $W_{q,r}$ | wavelet coefficient position |
| $T$ | the threshold value for hard and soft thresholding |
| $p$ | total pixel counts |
| $\delta$ | noise variance |
| $H, W \text{ and } C$. | height, width, and channel |
| $X_{pat}^{(i,j)}$ | patch embedding |
| $X_{hor}^{(i)}$ | Horizontal strip embedding across anatomical layers |
| $X_{\upsilon}^{(j)}$ | vertical strip embedding |
| $f(\cdot)$ | HoVer-Transformer block |
| $\{Z_h^{l,k}, Z_\upsilon^{l,k}, Z_{h2\upsilon}^{l,k}, Z_{\upsilon 2h}^{l,k}\}$ | features output |
| $\tilde{S}^{-\frac{1}{2}}\tilde{A}\tilde{S}^{-\frac{1}{2}}$ | aggregation matrix |
| $\tilde{S}$ | degree matrix |
| $H^{(g)}$ | node feature matrix |
| $\sigma$ | activation function |
| $L^{(g)}$ | modified lapalcian |
| $Q$ | query |
| $K$ | key |
| $W^Q, W^K$ | projection matrices |
| $\phi(\cdot)$ | implicit kernel mapping function |
| $P^C$ | $C - order$ of $P$. |
| $U_{best}$ | best solution |
| $Fp_i$ | fish positions |
| $U_x$ | Osprey's position |
| $u_{i,j}^{P2}$ | New Osprey's position |

## 1. INTRODUCTION

Among the leading causes of death on a global scale, leukemia is a deadly subtype of cancer-related disorders that can afflict both adults and kids of any age [1]. In particular, it is linked to the destruction of bone marrow by WBC and the ensuing increase in the number of immature lymphocytes. Therefore, to improve survival chances, a good cancer treatment plan must include an accurate and prompt cancer diagnosis [2]. Acute leukemia is a grave illness characterized by an abrupt rise in the person's blood leukemic cell count. A standard bone marrow investigation will indicate a low number of normal WBCs and a significant amount of leukemic cells. Symptoms of acute leukemia in patients may include recurrent infections, tiredness, and easy bruising. Persistent leukemia, on the other hand, typically advances slowly [3]. To further identify both acute and chronic blood tumors, examine the cell types impacted by the disorders. This further categorization establishes whether lymphoid or myeloid cells that cause leukemia [4]. While lymphoid leukemia cells collect and result in lymph node enlargement, Granulocytic, and myeloid sarcomas are created when myeloid leukemia cells group together [5].

Leukemias that are acute myeloid (AML), chronic (CML), acute lymphoblastic (ALL), and chronic lymphoblastic leukemia (CLL) are the four most common forms of leukemia [6]. The most prevalent leukemia, known as ALL, advances quickly and can be identified by an abundance of young lymphocyte cells in the picture of the blood sample [7]. Microscopically, ALL lymphocytes are small, homogenous, spherical blast cells with single nucleoli in the nucleus and scant cytoplasm [8]. Children under a year old are usually affected by AML, a heterogeneous malignant myeloid.

Oval in shape, leukemic cells in AML might contain Auer rod-shaped components in their broader granular cytoplasm [9].

The current method for diagnosing this illness involves manually analyzing blood samples that were collected using microscopic imaging; this process is frequently highly slow, tedious, and less precise [10]. Several deep-learning methods are employed to address these problems, and leukemic cancer identification and classification have been studied extensively [11]. According to some academics, the segmentation technique should be used to extract accurate characteristics from the divided ROI (region of interest) portion of the blood smear images. In particular, there are three main categories of segmentations used for leukemic illness: pixel-based, region-based, and shape-based [12]. Furthermore, leukemic cell analysis uses a variety of feature extraction techniques. These consist of edge features and morphological characteristics like form. Moreover, geometrical and statistical data, together with textural, color, and GLCM aspects, are used [13]. Similarly, various classifiers have been utilized to classify leukemic cells from normal cells. Many issues and difficulties in image analysis have now been resolved with the advent of deep learning since these methods made use of computerized feature engineering [14]. Because deep learning methods yield excellent precision and reduce computational costs, in the detection of leukemia cancer, they perform superior to conventional machine learning techniques [15]. In order to identify leukemia utilizing microscopic blood samples, an efficient hybrid deep learning framework is thus suggested. The following is a list of the suggested research work's principal contributions:

- In order to classify white blood cancer cells using microscopic images of bone marrow, a novel optimal deep learning model is developed.
- Initially, the raw blood smear images are collected from two publically available datasets namely, SN-AM and ALL-IDB in the image acquisition stage.
- Secondly, the collected raw blood sample images are filtered using a pre-Gaussian discrete Wavelet transformer to remove the background noise and to improve the quality in the pre-processing stage.
- Then, the cancer-affected region is segmented using the Anatomy-Aware Hover Transformer.
- After segmentation, the critical features needed for precise categorization are extracted and the types of cancer are detected and classified using a hybrid Similarity-Navigated Graph Diffusion Kernel Attention Network (SNGDKANet).
- Lastly, several metrics are utilized to assess the performance of the built model, including sensitivity, specificity, f1-score, accuracy, recall, and precision. Also, the efficiency of the provided model is tested using ALL-IDB and SN-AM datasets.

The innovation in the new approach is the incorporation of a hybrid deep learning model that merges the Similarity-Navigated Graph Neural Network (SNGNN) with a Diffusion Kernel Attention Network (DKAN) to create the new SNGDKANet model, which is designed specifically for the categorization of cancerous WBC. In contrast to conventional approaches based on labor-intensive feature extractions or shallow CNN-based models, the presented method in this work adopts a high-level similarity-driven graph approach to encode inter-cellular and high-dimensional feature dependencies. The utilization of Anatomy-Aware Hover Transformer (AAHT) for accurate region-based segmentation and optimization of hyperparameters using the bio-inspired Osprey Optimization Algorithm (OOA) also differentiates the model. This combined and streamlined architecture has resulted in higher classification accuracy, smaller error rates, and faster computation, thus overcoming the critical shortcomings of misclassification, high processing time, and low detection performance exhibited by current approaches.

### *1.1 Problem Statement*

The categorization of cancerous WBCs from blood samples poses a number of difficulties for traditional machine-learning algorithms. The morphological heterogeneity of WBCs can cause misclassification and make proper classification more difficult, both within and between patient populations. Consequently, there is a significant increase in the death rate. Additionally, the diagnosis process is delayed by the long execution time and low detection rate.

### *1.2 Motivation*

Deep Learning models can develop a robust system that effectively distinguishes white blood cancer cells and typical WBCs with excellent precision and effectiveness. In this research, a novel Similarity-Navigated Graph Diffusion Kernel Attention Network (SNGDKANet) is employed to classify normal cells and white blood cancer cells and their categories. The proposed SNGDKANet model integrates an SNGNN with a DKAN to perform classification. Therefore, SNGNN effectively leverages cell feature similarities for precise message passing that enhances classification accuracy and DKAN uses diffusion kernels to focus on relevant features for accurate white blood cancer cell classification.

The remaining of this study is arranged as: A few studies that are pertinent to the proposed study being presented are discussed in Section 2. A brief explanation of the recommended methodology is explained briefly in Section 3. Simulation results with considerations are given in Section 4. Finally, the presented research work is finished in Section 5 with a discussion of possible future research directions.

## 2. RELATED WORKS

A few contemporary works of literature studies relevant to the proposed research work are reviewed as follows:

Ramasamy et al. [16] offered a hybrid method to ascertain the kind of cancer found in the bone area by using a deep CNN. To maximize the CNN hyperparameters, adaptive multi-objective CAT approaches are applied. After that, an Optimized Convolutional Neural Network (O-CNN) is trained using the suggested model to recognize and categorize the various cancer types. The efficacy of the developed model is evaluated using the SN-AM dataset and several performance metrics, including accuracy, specificity, and F1-score.

Devi et al. [17] utilized the Leaky Convolutional RELU with XGBoost and CatBoost (CLR-CXG) architecture to divide up the images and take out the key characteristics for categorization. CLRXG is intended to enhance performance and accelerate the processing of forecasting tasks involving regression or classification. Reduced bias and excellent accuracy are the objectives of this CLRC implementation. As a result, the test images are classified as either acute lymphoblastic leukemia (ALL) or multiple myeloma (MM) via the CLR-CXG.

Raghaw et al. [18] created the CoTCoNet, or Coupled Transformer Convolutional Network, to classify leukemia. Dual-feature extraction is used with the CoTCoNet under discussion to collect several universal and fine-grained hematologic characteristics. It utilizes a graph-based framework and a population-specific meta-heuristic approach to select and improve attributes in order to find biologically significant features in leukocyte cells.

Gokulkannan et al. [19] created a powerful framework for deep learning for the identification of leukemia. Images from conventional leukemia datasets are segmented using a hybrid Multi-scale Trans-Res-Unet3+ Network (MTResUnet3+). The most pertinent features are chosen by using a Chameleon Swarm Algorithm Based on Elections (E-CSA) after important attributes such as color, form, and texture have been retrieved. E-CSA enhances the parameters of the model to raise detection precision. The chosen features are fed into a Multi-scale Dilated Convolutional Neural Network with Adaptive and Attentional Features (MAA-DCNN) to identify blood cancer.

Abhishek et al. [20] used a hybrid approach for classifying acute leukemia using a heterogeneous dataset of 500 photos from peripheral blood samples, including images of normal acute myeloid leukemia and ALL. Deep learning and machine learning methods are combined in the hybrid model. Using the diverse dataset, tasks related to binary-class and three-class classification are automatically finished. Here, three-class categorization using ResNet-50 comes after binary-class classification using VGG-16 and DenseNet employing support vector machines (SVM).

Balasubramanian et al. [21] offered a cutting-edge hybrid approach based on SVM and modified Unet for identifying WBC. To segment WBC, features are extracted and classified from a modified Unet architecture using support vector machines for radial basis functions (RBF-SVM). The results of the experiments showed that the enhanced Unet segmentation has a large dice similarity coefficient and can identify the WBC nucleus with excellent accuracy.

Batool and Byun. [22] offered an EfficientNet-B3-based efficient model that uses convolutions with depth-wise separability in the WBC images to differentiate between healthy cells and ALL. It has been suggested that using fewer trainable parameters, the EfficientNet-B3 will improve leukemia classification performance and efficacy. Moreover, the efficacy and generalizability of EfficientNet-B3 are evaluated on two publicly available datasets.

Khan et al. [23] used generative adversarial networks (GANs) for the concurrent classification and segmentation of platelets (PLTs), WBCs, and red blood cells (RBCs). The mapping between a confidence map and a WBC picture is determined by the network generator. To emphasize the distinctions between the confidence map and the images of microscopic blood cells, the network's discriminator is crucial. The presented model greatly improves bloodstream element categorization and segmentation when in contrast to cutting-edge techniques.

To fill a knowledge gap and meet the demand for a thorough viewpoint across a range of application domains, Ullah et al. [24] examine 155 articles on Explainable Artificial Intelligence (XAI) methodologies. For the significance of explainable AI in healthcare, Ullah et al. [25] demonstrated by the Brain Tumor Deep Explainable Deep Network (DeepEBTDNet), a deep learning model for early brain tumor identification that achieved 94.0% testing accuracy and 98.96% validation.

A deep learning model called DeepCRINet was created by Ullah et al. [26] to accurately identify lung diseases using chest radiography images (CRIs). It shows versatility in identifying diseases like tuberculosis, pneumonia, COVID-19, and lung opacity, overcoming constraints like dataset bias and underrepresentation. Using chest radiograph images, Ullah et al. [27] suggest a lightweight, dependable ChestCovidNet network for COVID-19 detection. With its 11 learning layers, layers that are fully linked and convolutional, the low-power model performs better than hybrid approaches and attains higher classification accuracy.

A lightweight Deep Learning framework called the Deep Tomato Detection Network (DTomatoDNet) was created by Ullah et al. [28] for the effective categorization of tomato leaf diseases. With 10,000 photos of tomato leaves and 19 learnable layers, it achieves 99.34% classification accuracy. For quicker disease identification, mobile applications can incorporate this simple method. For the early identification and categorization of lung conditions such as lung opacity, COVID-19, TB, and pneumonia, the DeepLungNet deep learning model is suggested by Ullah et al. [29] In the end, this approach improves healthcare overall by increasing possibilities for treatment and patient survival and limiting the transmission of infectious diseases.

On a typical Kaggle brain tumor MRI dataset, the TumorResnet deep learning model developed by Ullah et al. [30] for brain identification using binary classification has a 99.33% accuracy rate, outperforming more recent frameworks. This automated method improves patient survival and treatment options by aiding in the early diagnosis of brain malignancies. Every year, thousands of deaths are caused by brain tumors making them a serious global health concern. Pituitary tumors, meningiomas, and gliomas are detected and classified using deep transfer learning (TL) algorithms. According to a study that tests nine TL classifiers that have already been trained, the Inceptionresnetv2 algorithm by Ullah et al. [31] performs better than the others. The performance of TL algorithms and hybrid techniques is compared in the study.

Haq et al. [32] created a program for the identification of lung nodules in CT scan images to surpass the limitation of detecting them during pre-cancerous phases. The program compares several images, offering radiologists more information for early diagnosis of cancer. Upon extensive training, CNN can reduce false positives. For the identification and counting of HT-29 cells in human colorectal cancer, Haq et al. [33] utilized a deep-learning approach. ResNet-50 evaluates the model's precision on the dataset, which consists of 566 images. The technology assists in improved colon cancer diagnostic procedures and early detection. In this paper, a machine vision approach for detecting lung tuberculosis from symmetric CT scan images is proposed by Haq et al. [34]. With a low execution time and the greatest accuracy of 99%, the Multi-Layer Perceptron is based on supervised learning classifiers and optimized features.

## 3. PROPOSED METHODOLOGY

The three main forms of blood cancers include myeloma, lymphoma, and leukemia. Children are primarily affected by ALL, a complex lymphoid malignancy derived from the two T and B-lymphoid progenitors. On the other hand, carcinogenic plasma cells that interfere with the capacity of bone marrow to create healthy blood cells are responsible for MM. Patient survival rates are greatly increased by prompt treatment, which makes early identification of these malignancies essential.

Conventional diagnostic methods typically involve analyzing blood samples; however, these approaches can be labor-intensive, time-consuming, and susceptible to human error. This underscores the need for more efficient and reliable diagnostic techniques to ensure quicker identification and treatment of blood cancers, ultimately enhancing patient outcomes. By integrating image processing techniques with deep learning architecture, the proposed study develops a novel blood cancer cell classification and segmentation framework for the accurate classification of blood cancer cells into B-Lineage ALL (B-ALL) and MM. The block diagram representing the steps in segmentation and classification of B-ALL and MM is depicted below in Figure 1.

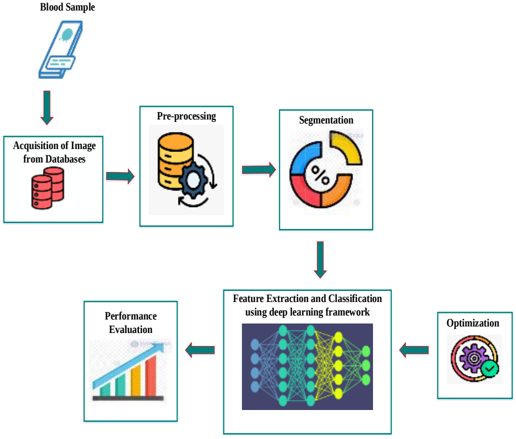

**Figure 1:** Block Schematic of Proposed Blood Cancer Segmentation and Classification Framework

Figure 1 provided above depicts the proposed deep learning-based methodology for segmenting and categorizing blood cancer cells. It includes a number of crucial steps, including the collection of images, pre-processing, segmentation, categorization, essential feature extraction, and optimization. At first, the input mages are collected from databases that contain patient's blood samples. After that, pre-processing is done on the images to enhance their quality and get them ready for analysis. After that, the processed images are segmented to isolate regions of interest, such as different cell types. After the images have been segmented, a deep learning model is employed to extract important features, which classifies them into B-ALL and MM. The classification model is optimized for improving performance. Finally, the framework's accuracy and efficiency are evaluated using metrics to assess its effectiveness.

### *3.1 Image Acquisition*

The patient's blood samples were used to obtain the raw microscopic pictures, which were gathered from two publicly accessible datasets: SN-AM and ALL-IDB. These collected images are used for segmenting and classifying the type of white blood cancer cells.

### *3.2 Pre-processing using Pre-Gaussian Discrete Wavelet Transformer based Filtering*

The raw input microscopic blood smear images taken from the datasets contain some unnecessary elements like noise, background, and red blood cells (RBCs). Therefore, these unwanted factors are removed and the input image is filtered to improve its clarity. So that it is easily analyzed. In this study, an efficient Pre-Gaussian Discrete Wavelet transformer (PGDWT) based Filtering [35] technique is employed in the pre-processing stage.

First, the image is smoothed and noise is reduced using Gaussian filtering, which preserves key image elements including edges and spatial information. This linear filter smooths the image and successfully removes random noise without noticeably distorting the key cell structures by averaging the values of pixels according to their separation from the center. After performing Gaussian filtering, a Discrete Wavelet Transformation (DWT) method is applied to further refine the image. DWT decomposes the image into different frequency components, allowing for the separation of high-frequency details from low-frequency information. This enables a more focused analysis of the features relevant to leukemia classification.

The Gaussian filter uses a constant matrix based on the Gaussian function $G_\rho$. It is given by,

$$G_\rho(q,r) = \frac{1}{2\pi\rho^2} e^{\frac{-q^2+r^2}{2\rho^2}} \qquad (1).$$

where, $q$ and $r$ denote pixel distances from the center and $\rho$ controls the smoothing level.

Thus, Gaussian filtering helps to average nearby pixel values thereby reducing random noise.

After smoothing, DWT decomposes the image into various frequency components, allowing for a more precise analysis. It is mathematically expressed as,

$$W_t(q,r) \le f(t), \lambda_{q,r}(t) \ge \int_R f(t)\hat{\lambda}_{q,r}(t)dt \qquad (2).$$

where, $f(t)$ represents the image function, and $\lambda_{q,r}(t)$ signifies the wavelet basis function.

To further reduce noise from the DWT coefficients, a thresholding method is applied. Generally, there exist two types of thresholding namely, soft thresholding and hard thresholding. The process of thresholding helps in enhancing the visibility of relevant features needed for precise classification. By converting grayscale images into binary formats, thresholding helps to isolate cellular structures, WBCs, for instance, from the backdrop. This is crucial for accurately identifying abnormalities and distinguishing between healthy and leukemic cells. It reduces noise and emphasizes the morphological characteristics necessary for analysis, thereby improving the performance of classification algorithms. Effective thresholding enables clearer segmentation and feature extraction thereby facilitating more precise classification leading to better diagnostic accuracy in leukemia detection.

At first, the process of soft thresholding is performed and is given by,

$$w'_{q,r} = \begin{cases} \operatorname{sgn}(w_{q,r})(|w_{q,r}| - T), & |w_{q,r}| \ge T \\ 0, & |w_{q,r}| < T \end{cases} \qquad (3).$$

here $W_{q,r}$ represents the wavelet coefficient position $(q,r)$, and $T$ defines the threshold value for hard and soft thresholding, If the magnitude of the noise is less than the predetermined threshold value, then it is set to zero.

$$w'_{q,r} = \begin{cases} w_{q,r}, & |w_{q,r}| \ge T \\ 0, & |w_{q,r}| < T \end{cases} \qquad (4).$$

If the value of the threshold is much smaller, then it passes to noisy components or if the value of the threshold is much higher it leads to loss of actual components in the image. To select a suitable threshold value, Donoho & Johnstone presented a universal threshold value applied on each wavelet coefficient. It is expressed as,

$$T = \delta\sqrt{2\log p} \qquad (5).$$

where, $\delta$ represents the noise variance and $p$ signifies total pixel counts.

Thus by using this combined approach in a pre-processing stage, the clarity and quality of blood smear images are enhanced leading to improved accuracy in leukemia detection.

### *3.3 Segmentation using Anatomy-Aware Hover Transformer*

In the segmentation stage, the cancer-affected portion from the images of blood smears is segmented to effectively analyze and categorize the cancer categories. In this concern, an Anatomy-Aware Hover Transformer (AAHT) [36] is employed to perform segmentation. The ROI (Region-of-Interest) portion to be segmented contains leukocytes and lymphocytes. The process of segmentation is of three types namely, segmentation by shape, segmentation by region, and segmentation by pixels.

In this work, the blood smear pictures are segmented using region-based segmentation to identify the cancer-affected area. Four modules make up the proposed AAHT model: a convolutional layer, a pooling layer, several blocks of HoVer-Transformers, and a flattening layer. Numerous HoVer-Transformer blocks, one pooling layer, and one convolutional block make up each module. Here, ConV blocks are used to combine both vertical and horizontal data. A 2D map of features serves as the input for every module. Attached to this is an embedding block that fits the input inside the transformer. In this instance, the input is embedded using three different embedding techniques: horizontal strip embedding, patch embedding and vertical strip embedding. The pooling layer in each module applies average pooling to make feature maps less dimensional. Finally, a fully connected layer performs inference and a segmented portion is received in the output block.

The presented model processes input blood smear images using a transformer architecture enhanced with anatomical prior knowledge. It uses embeddings to capture spatial relationships and features that are important for identifying cancerous areas. Figure 2 below shows the structure of the AAHT model:

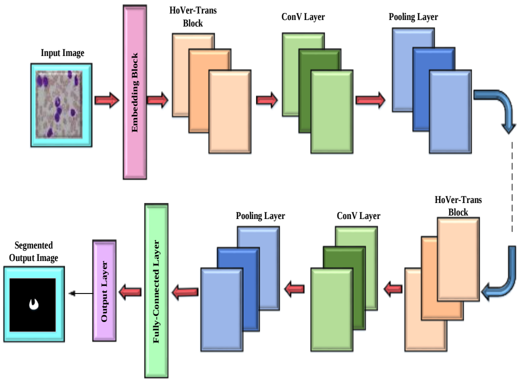

**Figure 2:** Schematic Structure of AAHT-based Segmentation Model

The layers in different stages of the AAHT model are explained as follows:

- **Embedding Layer**

The input image $X$ is first processed through a convolutional stem for performing down sampling and introduces early inductive bias. It is thus expressed as,

$$X' \in \mathbb{R}^{H/4 \times W/4 \times C} \qquad (6).$$

here the height, width, and channel were represented as $H, W \text{ and } C$. Then, the input image is fed into the model based on three embedding ways.

At first, patch embedding is performed in which the image is divided into $N \times N$ patches. It is expressed as,

$$Z_{pat} = \left\{ X_{pat}^{(i,j)} \middle| X \in \mathbb{R}^{H/4N \times W/4N \times C}, \quad i, j = 1, \ldots, N \right. \qquad (7).$$

here $X_{pat}^{(i,j)}$ represents the patch embedding at location (i, j). Then, horizontal embedding represents features from the identical layer of anatomy across $J$ strips and is described as,

$$Z_{hor} = \left\{ X_{hor}^{(i)} \middle| X \in \mathbb{R}^{H/4J \times W/4 \times C}, \quad i = 1, \ldots, J \right. \qquad (8).$$

here $X_{hor}^{(i)}$ indicates the Horizontal strip embedding across anatomical layers. Finally, vertical embedding captures features across different anatomical layers. It is thus expressed as,

$$Z_{ver} = \left\{ X_{\upsilon}^{(j)} \middle| X \in \mathbb{R}^{H/4 \times W/4J \times C}, \quad j = 1, \ldots, J \right. \qquad (9).$$

here $X_{\upsilon}^{(j)}$ denotes the vertical strip embedding.

- **HoVer-Trans Block**

The HoVer-Trans block has four branches: the H branch, the V branch, the H2V branch, and the V2H branch, which are used to record different spatial correlations. The V2H branch transforms vertical data into horizontal, the H2V branch transforms horizontal information into vertical, and the H branch focuses on horizontal features in this instance. Thus, the output features for the $k^{th}$ block in the $l^{th}$ stage are computed as,

$$\left\{ Z_h^{l,k}, Z_\upsilon^{l,k}, Z_{h2\upsilon}^{l,k}, Z_{\upsilon 2h}^{l,k} \right\} = f\left( Z_h^{l,k-1}, Z_\upsilon^{l,k-1}, Z_{h2\upsilon}^{l,k-1}, Z_{\upsilon 2h}^{l,k-1} \right) \qquad (10).$$

where, $f(\cdot)$ represents the HoVer-Transformer block and $\left\{ Z_h^{l,k}, Z_\upsilon^{l,k}, Z_{h2\upsilon}^{l,k}, Z_{\upsilon 2h}^{l,k} \right\}$ is the output of the feature from HoVer Transformer blocks in stage $l$ and block $k$.

The H and V branches capture spatial relationships between and between each HoVer-Trans block's levels. And, the H2V and V2H sections merge features gathered from the H and V branches. In this case, the H2V branch's counterpart is the V2H branch. It is therefore stated as,

$$Z_{h2\upsilon}^{l,k} = Trans\left( Trans\left( Z_h^{l,k} + Z_{h2\upsilon}^{l,k-1} \right) + Z_\upsilon^{l,k} \right) \qquad (11).$$

$$Z_{\upsilon 2h}^{l,k} = Trans\left( Trans\left( Z_\upsilon^{l,k} + Z_{\upsilon 2h}^{l,k-1} \right) + Z_h^{l,k} \right) \qquad (12).$$

here, are the features $Z_{h2\upsilon}^{l,k}$ and $Z_{\upsilon 2h}^{l,k}$ will be forwarded to the next block. In each stage, features from the final HoVer-Transformer layer are passed into the convolutional block.

- **Convolutional Layer**

A convolutional layer combines the output features to introduce inductive bias. Thus, the feature vectors $Z_{h2\upsilon}^{l,k}$ and $Z_{\upsilon 2h}^{l,k}$ are fused from 2 main transformer branches. It is expressed as,

$$Z^{l+1} = ConV\left( Z_{h2\upsilon}^{l,k} + Z_{\upsilon 2h}^{l,k-1} \right) \qquad (13).$$

The ConV block reshapes and concatenates the 1D feature vectors, processing them through three convolutional layers with varying channel numbers across stages.

By concentrating on significant areas of the image, the suggested AAHT model is a kind of artificial intelligence framework that segments the affected region by taking account of the anatomical structure and properties of blood cells. Strong spatial linkages between the characteristics are introduced by the transformer's self-attention nature. Thus, by considering the anatomy of blood cells, the AAHT model can more precisely identify cancerous regions, reducing misdiagnoses. Table 1 below describes the hyperparameters of the employed AAHT model.

Thus, the suggested architecture is designed to effectively segment cancer-affected portions from blood smear images by leveraging spatial features and anatomical knowledge. The model captures intricate relationships in the data, improving the accuracy of cancer detection. Thus, the combination of embeddings and a transformer with convolutional layers helps in identifying and segmenting affected regions, which is crucial for accurate medical diagnostics.

**Table 1:** Parameter setting of AAHT model

| **Parameter** | **Value** |
|---|---|
| Learning Rate | 0.0001 |
| Batch Size | 32 |
| Embedding Dimensions of each stage | $\{4,8,16,32\}$ |
| No. of HoVer Transformer blocks in each stage. | $\{2,4,4,2\}$ |
| Weight Decay | 0.1 |
| Head numbers of transformer blocks in each stage | $\{2,4,8,16\}$ |
| No. of Epochs | 250 |

### *3.4 Feature Extraction and Classification Using Similarity-Navigated Graph Diffusion Kernel Attention Network (SNGDKANet)*

The procedure for feature extraction helps in the precise categorization of cancer types by detecting and extracting the important characteristics in the blood smear image. A unique hybrid Similarity-Navigated Graph Diffusion Kernel Attention Network (SNGDKANet) is created in the suggested study to carry out feature extraction and classification. By reducing the amount of features in the feature extraction stage, the non-trainable layers aid in minimizing the computational cost of the suggested model. Here, the suggested framework separates the healthy and malignant photos based on the attributes retrieved. The proposed SNGDKANet model is obtained by combining a Similarity-Navigated Graph Neural Network (SNGNN) [37] with a Diffusion Kernel Attention Network (DKAN) [38]. Here, the combined model learns important features like shape, texture, and size from WBC images to effectively categorize the cancer types. The framework of the SNGDKANet model for feature extraction and categorization is illustrated in Figure 3:

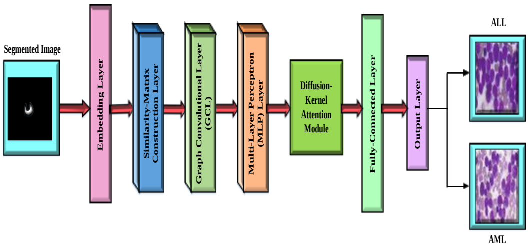

**Figure 3:** Architecture of SNGDKANet model for Classification and Feature Extraction

The architecture of the SNGDKANet model contains an embedding layer, an input layer, a similarity matrix construction layer, a graph convolutional layer (GCL), a multi-layer perceptron (MLP) layer, an output layer, and an attention layer. At first, the node features and adjacency matrix from the segmented input image are fed to the input layer. After that, an initial set of embeddings is created from raw node features by the embedding layer. Subsequently, a similarity matrix among nodes is computed by the similarity matrix building layer using their embeddings and network structure. The similarity matrix is used by the GCL to compile data from nearby nodes and update node embeddings. Utilizing the embeddings from previous layers, a similarity matrix integrating the graph structure and node features is constructed in each layer. Then, the MLP layer performs non-linear adjustments that improve node embeddings. The attention layer gives varying weights to node connections according to their significance, using the similarity matrix. Also, the attention layer focuses on important features that help in precise classification and improve the efficiency of the model. Finally, the classes representing the cancer categories are obtained at the output layer. The parameter setting of the hybrid SNGDKANet model is described below in Table 2:

**Table 2:** Parameter setting of the SNGDKANet model

| **Parameter** | **Value** |
|---|---|
| Learning Rate | 0.01 |
| Batch Size | 32 |
| No. of GCL | 2 |
| Dropout Rate | 0.2 |
| Embedding Dimension | 64 |
| Type of Kernel | Gaussian |
| No. of Attention Heads | 4 |
| Activation Function | ReLU |
| Loss Function | MSE |
| No. of Epochs | 200 |

Here, a regularization parameter namely, dropout is used to prevent over-fitting during the training process.

Initially, several similarity measurements are considered for extracting the key features from the segmented image. The measurements include node similarity matrix, neighborhood similarity, and class similarity for accurate detection and classification. Here, the high level of inter-class and intra-class similarity provides effective discrimination between classes.

Thus, a symmetric normalized adjacency matrix or aggregation matrix is obtained from the equation (14),

$$H^{(g)} = \sigma\left(\tilde{S}^{-\frac{1}{2}}\tilde{A}\tilde{S}^{-\frac{1}{2}}H^{(g-1)}M^{(k-1)}\right) \qquad (14).$$

where, $\tilde{S}^{-\frac{1}{2}}\tilde{A}\tilde{S}^{-\frac{1}{2}}$ represents the aggregation matrix which $\tilde{S}$ indicates the degree matrix.

It then substitutes the node similarity matrix for the adjacency matrix, which categorizes the neighborhood data in each layer. After that, the node similarity matrix can be obtained by modifying the dissemination and aggregation process, as shown by equation (15),

$$H^{(g)} = \sigma\left(L^{(g)}H^{(g-1)}M^{(k-1)}\right) \qquad (15).$$

where $H^{(g)}$ specifies the node feature matrix, $\sigma$ denotes the activation function, and $L^{(g)}$ modified lapalcian. Here, the proposed model is coupled with a DKAN that works well to focus on important features that offer precise cancer classification. The attention module, which is coupled to the convolutional layer of the SNGNN, comprises a position encoding block, a frontal linear input projection block, a completely linked layer, an average pooling layer, several stacked transformer encoder layers, and a Softmax function. The Softmax function is used to modify the similarity matrices created following the attention strategy. In order to maintain discriminative characteristics for class distinction according to the node similarity matrix, a novel intentionally aggregating approach is used here to choose similar neighbors.

The position encoding layer in the attention module maps each region of interest portion into a real-valued U-dimensional vector. Thus, the resultant encoding matrix is represented as $E \in \mathbb{R}^{N \times T \times U}$.

Here, each transformer encoder layer transforms the features that are expressed as,

$$Y_g = f_g\left(a_g\left(\left(Y_{g-1}\right), Y_{g-1}\right)\right), \quad g \in 1, \ldots\ldots, G \qquad (16).$$

The self-attention module in DKAN takes $Y_{g-1} \in \mathbb{R}^{N\times T\times U}$ as input and generates the query, key, and value tensors in the $g^{th}$ layer. Thus, the three components are represented as,

$$Q = Y_{g-1} D^{Q} \tag{17.}$$

$$K = Y_{g-1} D^{K} \tag{18.}$$

$$K = Y_{g-1} D^{V} \tag{19.}$$

here, both query and key tensors are reshaped into $N \times TU_l$ dimensional matrices for calculating attention coefficients. Therefore, the self-attention in $g^{th}$ layer is expressed as,

$$a_g\left(Q,K,V\right) = V' = soft\max\left(\frac{QK^{T}}{\sqrt{TU_k}}\right)V \tag{20.}$$

In the above equation (20), the matrix $QK^{T}$ is denoted as a $N \times N$ dimensional matrix and is expressed as,

$$A_{x,y} = \left\langle q_x, k_y \right\rangle = \left\langle i_x W^{Q}, i_y W^{K} \right\rangle \tag{21.}$$

where, $W^{Q}, W^{K}$ denotes the projection matrices and $i_x, i_y$ represents the $x^{th}$ and $y^{th}$ rows of $Y_{g-1}$.

The equation (21) expressed above measures the dependency between projected features and region of interest features in $x^{th}$ and $y^{th}$ rows.

A non-linear kernel is then used to measure the similarity, thus the above equation is rewritten as,

$$\begin{aligned} A_{x,y} &\Rightarrow \left\langle \phi(i_x), \phi(i_y) \right\rangle \\ &= k(i_x, i_y) \\ &= K_{x,y} \end{aligned} \tag{22.}$$

where, $\phi(\cdot)$ signifies an implicit kernel mapping function that maps the input feature $i$ onto a feature space with more dimensions.

Finally, the attention matrix of the kernel is represented as,

$$K_{bC} = P^{C} K \tag{23.}$$

where, $P^{C}$ represents the $C-order$ of $P$.

Finally, a weighted sum is used to aggregate the several diffusion kernel attentions; the weights are adaptively learned during training to accomplish the particular job.

The loss function of the suggested deep learning model is minimized by fine-tuning its weight and bias parameters. In this study, Mean-Square Error (MSE) is considered as a loss function that is to be reduced for achieving improved performance during classification. The MSE loss function is expressed as,

$$MSE = \frac{1}{N_P}\sum_{x=1}^{N_P}\left(G_x - P_x\right)^2 \tag{24.}$$

where $N_P$ refers to the amount of image pixels, $G_x$ signifies ground truth image, and $P_x$ indicates the image that is predicted.

The loss function expressed in equation (24) is to be optimized to increase the classifier model's effectiveness. The application of MSE as the loss function in this research guarantees accurate optimization by penalizing deviations between predicted and true labels that are larger than a few units. MSE promotes smoother updates of the gradients, hence achieving stable convergence during training. The optimized MSE directly contributes to fewer classification errors. Therefore, the model attains greater accuracy and better generalization on unseen leukemia images. While the choice of MSE is more unusual than choosing the Binary Cross Entropy, it could be explained by an empirical approach. In effect, this error worked for smooth convergence and better generalization when coupled with graph-based representation and attention mechanisms in the SNGDKANet model. An experiment in comparison proved that while BCE gained slightly faster properties of early training, MSE pressed to a higher final accuracy (98.9% vs. 97.8%) and to a lower error rate (1.1% vs. 2.2%) in the C-NMC 2019 dataset. This stands as evidence of why MSE is more suitable for detecting subtle deviations of features in the fine-grained classification of medical images. Hyperparameter optimization for the proposed model is carried out by employing a novel meta-heuristic optimization Osprey Optimization Algorithm (OOA) [39].

### *3.4.1 Optimization of Hyper Parameters Using OOA*

The deep learning model's hyperparameters help in controlling the training process. Therefore, these parameters are to be fine-tuned to raise the model's overall effectiveness and classification accuracy. In the proposed study, the hyperparameters of the classifier model are optimized by utilizing OOA. The suggested OOA is motivated by the hunting behavior of ospreys. Ospreys dive to catch fish with remarkable accuracy, adjusting their position and speed dynamically. This algorithm emulates this adaptive, focused search strategy in optimization problems, balancing exploration and exploitation. Like an osprey's hunting, the algorithm hones in on promising solutions while maintaining a broad search to avoid local optima. The steps in the presented OOA are described below:

***Step 1: Initialization***

This phase initializes the population size, upper and lower boundaries, and the maximum number of iterations. Furthermore, osprey positions within the search space are randomly initialized. Thus, the process of initialization is modeled as,

$$U = \begin{bmatrix} U_1 \\ \vdots \\ U_i \\ \vdots \\ U_{N_P} \end{bmatrix}_{N_P \times h} = \begin{bmatrix} u_{1,1} \cdots u_{1,j} \cdots u_{1,h} \\ \vdots \quad \ddots \vdots \quad \iddots \vdots \\ u_{i,1} \cdots u_{i,j} \cdots u_{i,h} \\ \vdots \quad \iddots \vdots \quad \ddots \vdots \\ u_{N_P,1} \cdots u_{N_P,j} \cdots u_{N_P,h} \end{bmatrix}_{N_P \times h} \quad (25).$$

$$u_{i,j} = LB_j + k_{i,j} \cdot (UB_j - LB_j),\ i = 1,2,\ldots..,N_P,\ j = 1,2,\ldots.,h \quad (26).$$

where $u_{i,j}$ represents the $i^{th}$ candidate solution in $j^{th}$ dimension, $N_P$ denotes total search agent counts in search space, and $k_{i,j}$ represents a random number in the interval [0, 1].

***Step 2: Calculation of fitness function***

To determine which solution is optimal, the objective function measurement for every potential solution is assessed. The fitness function is evaluated using below equation (27),

$$Fitness(F^*) = Max(\eta) \cdot Min(\varepsilon) \quad (27).$$

where, $\eta$ represents the classification accuracy and $\varepsilon$ indicates the error rate.

In the above fitness equation (27), the accuracy is maximized and the rate of error is reduced to attain the best optimal solution.

***Step 3: Identifying the position of fish and hunting it (Exploration phase)***

In OOA, the exploration phase involves various strategies like identifying the fish, attacking the fish, and updating of position.

According to the first strategy, a set of fish for each search agent is found using equation (28),

$$Fp_i = \{U_x | x \in \{1,2,\ldots.,N_P\} \wedge F_x < F_i\} \cup \{U_{best}\} \quad (28).$$

where $Fp_i$ denotes a set of fish positions for $i^{th}$ search agent, $U_x$ represents the position of $x^{th}$ osprey, and $U_{best}$ indicates the best solution. Then, the location of the osprey is updated if the new position has improved objective function value. Then, the position is updated using equation (29),

$$U_i = \begin{cases} U_i^{P1}, \ if \ \ F_i^{P1} < F_i; \\ U_i, \ \ else \end{cases} \quad (29).$$

where, $U_i^{P1}$ indicates the new position of $i^{th}$ osprey due to the exploration phase and $F_i^{P1}$ denotes the fitness function's value at the new position. Thus, the process of exploration helps the search agents escape local optima and move closer to the global optimum.

***Step 4: Carrying fish to an appropriate position (Exploitation phase)***

The exploitation behavior in OOA is inspired by the osprey's behavior of carrying a caught fish to a safe spot to eat, which leads to small adjustments in the osprey's position. This process helps the algorithm to refine its search and converge toward better solutions. The exploitation process is carried out based on finding a suitable position to eat the fish and updating of position. After catching a fish, the osprey attempts to move to a nearby position to eat that fish. Then, the new position is adjusted to ensure that the ospreys stay within the boundaries of the search space. It is formulated as,

$$u_{i,j}^{P2} = \begin{cases} u_{i,j}^{P2}, \ if \ LB_j \le u_{i,j}^{P2} \le UB_j; \\ LB_j, \ if \ u_{i,j}^{P2} < LB_j; \\ UB_j, \ if \ u_{i,j}^{P2} > UB_j. \end{cases} \quad (30).$$

where, $u_{i,j}^{P2}$ denotes the new position of $i^{th}$ osprey on dimension $j$ due to exploitation strategy The program then assesses if the new position provides an improved function value after determining the new position. If so, the following equation (31) is used to update the osprey's position.

$$U_i = \begin{cases} U_i^{P2}, \ if \ \ F_i^{P2} < F_i; \\ U_i, \ \ else \end{cases} \quad (31).$$

where, $U_i^{P2}$ denotes the new position of $i^{th}$ osprey due to the stage of exploitation and $F_i^{P2}$ shows the intended function value at the new position.

Thus, the exploitation phase makes the algorithm more capable of fine-tuning the results and converging on the optimal solution.

***Step 5: Determination of best solution***

The best ideal solution is estimated by selecting the candidate with the highest fitness value (i.e. high classification accuracy and less error rate).

***Step 6: Termination***

Finally, the presented OOA is terminated after reaching a maximum quantity of iterations.

In the presented OOA, the size of the population is set to 100, and maximum iteration counts are set to 1000.

The Pseudocode representing the hyperparameter optimization using OOA is given below in Table 3. Table 3 shows that Algorithm for Osprey Optimization Algorithm.

**Table 3:** Algorithm for Osprey Optimization Algorithm

```
Start OOA
Input: Objective Function, Decision Variables, and Constraints.
Set the size of the population $(N_P)$ and maximum iteration counts $(I)$.
Create the initial population using (25) and (26).
Calculate fitness function using (27).
For $t = 1$ to $I$
    For $i = 1$ to $N_P$
        Phase 1: Exploration
        Update the position to find a set of fish locations using (28)
        Determine the position of fish selected randomly by osprey.
        Estimate the new position of search agents using (29).
        Check the boundary for a new position within the search location using (30).
        Update the position of the osprey using (31).
        Phase 2: Exploitation
        Estimate the new position of search agents based on exploitation strategy using (32).
        Evaluate the boundary conditions for the estimated new position using (33).
        Update the position of $i^{th}$ osprey using (34).
end
Save the best optimal solution found.
Output: Optimal best solution with high accuracy and less error rate.
End OOA.
```

### *3.4.1.1 Computational complexity of OOA*

The complexity of computing of OOA relies on the establishment and update of positions process based on the exploration and exploitation strategies. The initialization's computational complexity stage is $O(N_P h)$, where $N_P$ denotes the size of the population and $h$ denotes the number of problem variables. Then, the position update process's computational complexity based on exploration and exploitation behaviors is $O(2N_P hI)$ in which $I$ signifies maximum iteration counts. Therefore, the overall complexity of OOA is $O(N_P h(1+2I))$.

Thus, the developed framework uses the relationships between cells in images to effectively extract features and classify them, resulting in improved white blood cancer cell identification and categorization.

## 4. RESULTS AND DISCUSSION

The model that is being presented is run in the Python version 3.8 programming language. The suggested model's effectiveness is evaluated using the ALL-IDM and SN-AM datasets. Additionally, the effectiveness of the built model is assessed by contrasting its metrics values with those of a few cutting-edge deep learning models that are currently in use, including O-CNN, CoTCoNet, MAA-DCNN, Duplet-CNN, Resnet-50, EfficientNet-B3, Unet and RWP-GAN. To ensure transparency and reproducibility of the proposed segmentation and classification framework, Table 4 presents a detailed summary of the optimized hyperparameters used in the AAHT, the SNGDKANet, and OOA.

All experiments were carried out on a high-performance computer system in order to verify the effectiveness and performance of the suggested SNGDKANet-based framework. The complete hardware and software environment utilized for assessment, testing, and training is summarized in Table 5. These settings ensure consistent reproducibility and align with standard practices in deep learning-based medical image analysis.

**Table 4:** Summary of Optimized Hyperparameters for the Proposed Model

| **Component** | **Hyperparameter** | **Optimized Value** |
|---|---|---|
| AAHT (Segmentation) | Learning Rate | 0.0001 |
| | Batch Size | 32 |
| | Weight Decay | 0.1 |
| | No. of HoVer-Transformer Blocks (per stage) | [3, 3, 3, 3] |
| | Embedding Dimensions (per stage) | [64, 128, 320, 512] |
| | No. of Attention Heads (per stage) | [2, 4, 5, 8] |
| | Epochs | 250 |
| SNGDKANet (Classification) | Learning Rate | 0.01 |
| | Batch Size | 32 |
| | No. of Graph Convolution Layers (GCL) | 2 |
| | Dropout Rate | 0.2 |
| | Embedding Dimension | 64 |
| | Kernel Type | Gaussian |
| | No. of Attention Heads | 4 |
| | Activation Function | ReLU |
| | Loss Function | MSE |
| | Epochs | 200 |
| OOA | Population Size | 100 |

| | | |
|---|---|---|
| (Optimization) | | |
| | Max Iterations | 1000 |
| | Exploration Strategy Parameters | Random Initialization |
| | Exploitation Strategy Parameters | Local Search Update |

**Table 5:** Experimental Setup and Configuration Details

| **Category** | **Specification** |
|---|---|
| Processor | Intel® Core™ i7-12700K @ 3.60 GHz, 12 Cores |
| RAM | 32 GB DDR4 |
| GPU | NVIDIA GeForce RTX 3080 (10 GB GDDR6X) |
| Storage | 1 TB NVMe SSD |
| Operating System | Windows 11 Pro 64-bit |
| Programming Language | Python 3.8 |
| Deep Learning Framework | TensorFlow 2.11 / PyTorch 1.13 (Specify depending on usage) |
| Supporting Libraries | NumPy, OpenCV, Scikit-learn, Matplotlib, Pandas |
| Optimization Tool | Custom implementation of Osprey Optimization Algorithm (OOA) |
| Dataset Split | 70% Training, 30% Testing |

The training of the presented method is a supervised training that occurs by using labeled microscopic blood smear images from the datasets ALL-IDB and SN-AM. The unprocessed images are first pre-processed through PGDWT to eliminate noise and enhance image quality, after which region-based segmentation operating through AAHT isolates the cancer-affected areas. Subsequently, these segmented regions provide the construction of graph representations that are used as input to the SNGDKANet in order to extract and classify features. During the training, backpropagation, node embedding, and attention weights are learned by the model while being monitored by the MSE loss function. The OOA-based optimization process dynamically adjusts meta-parameters like learning rate or dropout towards minimizing the loss value. The parameters trained are optimized over 200 epochs for classification, 250 epochs for segmentation, and a batch size of 32, with the ReLU activation and the Gaussian kernel being used for calculating attention values. To ensure that the model works well when applied to fresh, untested data, the next step is to evaluate the model's performance using a 70:30 train-test split.

### *4.1 Dataset Description*

Three publicly available datasets, SN-AM (Sanguinaria and Neutrophil-Aggregate Microscopy), C-NMC 2019, and ALL-IDB (All India Institute of Medical Sciences Image Database), are used to evaluate the efficacy of the suggested method.

#### *4.1.1. SN-AM dataset (https://www.kaggle.com/datasets/pussydestroya69/sn-am-final?select=train)*

The bone marrow aspiration method is used to obtain the microscopic pictures in this collection from patients. The bone marrow slides of patients with B-ALL and MM. Images in BMP format with a pixel size of 2560 × 1920 make up the dataset. The dataset includes 90 pictures of B-ALL and 100 pictures of MM, with notable inter-image variability.

#### *4.1.2. ALL-IDB dataset*

The Acute Lymphoblastic Leukemia -ImageDataBase (ALL-IDB) data set (https://homes.di.unimi.it/scotti/all/), publicly available on the internet, supplied the images in this study. Two forms of this data set were developed. The 108 photographs of ALL-IDB-1 contained 49 leukemia patient photographs and 59 photographs of healthy individuals. The 260 single-cell images in the ALL-IDB 2 dataset consisted of 130 leukemia patient images and 130 control images. These images are of resolution 257x257 and a color depth of 24 bits. In ALL-IDB-2, for the further classification of the leukemia cells the subtypes were labeled as L1, L2, and L3.

#### *4.1.3. C-NMC 2019 dataset*

The C-NMC 2019 dataset (https://www.kaggle.com/gauravrajpal/leukemia-classifcationv1-3-inceptionv3-65-29/data) consists of images of 15114 lymphocytes from 118 individuals. Three folders contain the images: "C-NMC training data" contains 10,661 cells, of which 7,272 are malignant cells from 47 subjects and 3,389 are healthy cells from 26 subjects; "CNMC test preliminary phase data" contains 1,867 cells from 13 subjects (1,219 malignant cells and 648 healthy cells from 15 subjects); and "C-NMC test final phase data" contains 2,586 unlabeled cells from 17 subjects. Expert oncologists have already labeled single-cell photos of benign and malignant cells in these folders.

30% of the blood sample photos in this study are used for testing, while the remaining 70% are used for training. The C-NMC 2019, SN-AM, and ALL-IDB datasets used in this study were thoroughly examined and found to contain no missing data, as each sample includes complete image and label information. However, minor outliers were observed in terms of image quality and staining variations. These were effectively handled through preprocessing using PGDWT to enhance consistency.

### *4.2 Performance Evaluation*

The efficiency of the recommended model is evaluated using some standard measures, including implementation or run time, f1-score, recall, specificity, accuracy, precision, sensitivity, and error rate. These metrics are computed using the following formulas in Table 6.

The parameters expressed in the above equations are defined as

- **True Positive** $ab$**:** Accurately forecasts as normal.
- **False Positive** $db$**:** False positives mistakenly classify normal as aberrant.
- **False Negative** $dc$**:** A false negative is when an unhealthy state is unexpectedly interpreted as normal.
- **True Negative** $ac$**:** Exceptionally precise forecasts of anomalous cases.
- **Area under the Curve** (**AUC):** The effectiveness of the binary classification technique in differentiating between cancerous and normal cells is measured by AUC.
- **Matthew's Correlation Coefficient (MCC):** This statistic is employed to evaluate a deep learning model's accuracy.

**Table 6:** Performance Matrices and Equations

| **Performance Metrics** | **Equation** |
|---|---|
| Accuracy | $\frac{ab+ac}{ab+ac+db+dc}$ |
| Sensitivity | $\frac{ab}{dc+ab}$ |
| Specificity | $\frac{ac}{db+ac}$ |
| Precision | $\frac{ab}{ab+db}$ |
| Recall | $\frac{ab}{ab+dc}$ |
| AUC | $\frac{1}{2}\left(\frac{ab}{(dc+ab)}+\frac{ac}{(ac+db)}\right)\times 100$ |
| MCC | $\frac{(ab\times ac-db\times dc)}{\sqrt{((ab+db)(ab+dc)(ac+db)(ac+dc))}}\times 100$ |
| F1-score | $2\times\frac{n\times m}{n+m}$<br>Where, $n$ denotes the precision, $m$ is the recall. |

Among the performance indicators that were chosen were execution time, F1-score, specificity, accuracy, precision, recall, AUC, and error rate —which are an all-encompassing measure of the model's diagnostic performance. Accuracy is not indicative enough in imbalanced sets; therefore, precision and recall tell us about false positives and false negatives, which are of paramount importance in medical diagnosis. The F1-score gives equal weight to these, providing a trustworthy measure even with class imbalance. Specificity measures the model's capability to accurately label healthy cases, whereas AUC estimates its discriminative ability. Error rate and run time estimate reliability and practical applicability, particularly for real-time clinical use. These measures taken together guarantee statistical reliability as well as clinical utility.

The obtained metrics values are compared with a few state-of-the-art existing approaches to assess their efficiency.

**Table 7:** Output Results of ALL-IDB dataset

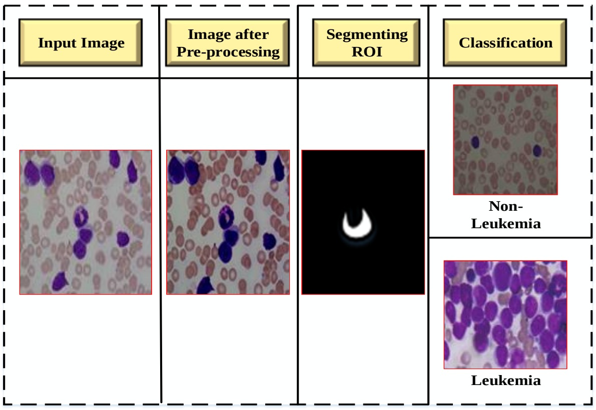

The above table 7 shows the output results from the ALL-IDB dataset for classifying cell images. The first column shows the input image, which undergoes pre-processing in the second column to enhance features. The third column highlights the segmented region of interest (ROI), identifying critical areas for analysis. The fourth column displays the classification result, distinguishing between healthy cells (non-leukemia) and ALL cells (leukemia) based on the processed data.

The above table 8 shows the output results from the SN-AM dataset for classifying cell images. The first column shows the input image, which undergoes pre-processing in the second column to enhance features. The third column highlights the segmented region of interest (ROI), identifying critical areas for analysis. The fourth column displays the classification result, distinguishing between B-ALL (B-Lineage Acute Lymphoid Leukemia) and MM based on the processed data.

**Table 8:** Output Results of SN-AM dataset

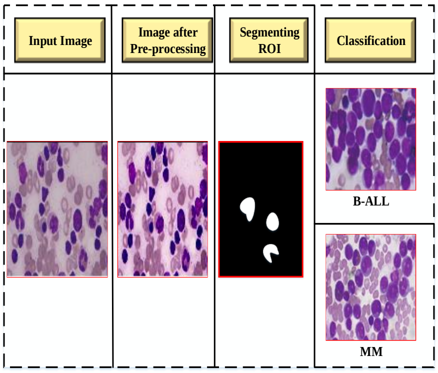

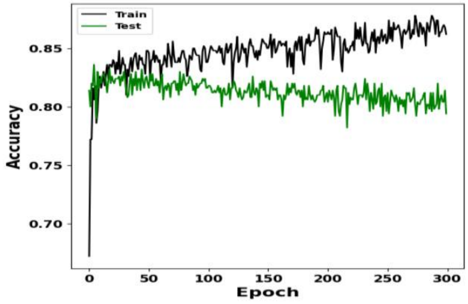

**Figure 4:** Training Vs Testing Accuracy under the SN-AM dataset

Figure 4 shows the testing and training accuracy of the suggested framework over 300 epochs. After 50 epochs, the training accuracy grows quickly from a starting point of about 72%. Although it gradually rises, the testing accuracy never reaches the training accuracy. Despite this, both accuracies exhibit steady trends that suggest the model picks up cancer category distinctions more quickly. The model proposed demonstrates fast convergence in the first 50 epochs, which is a sign of effective feature learning. The steady increase in training accuracy with a closely following testing accuracy curve proves the model's robust generalization capability. The tiny contrast between the two demonstrates that the model is stable across a range of SN-AM dataset samples and is not overfitting.

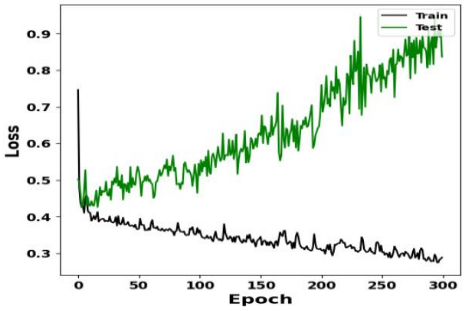

**Figure 5:** Training Vs Testing Loss under the SN-AM dataset

Figure 5 shows the loss for both the training and testing sets over 300 epochs. The training loss starts near 45 % and steadily decreases, reaching approximately 30% by the 300th epoch. This shows how well the model performed using the training set of data improves steadily. However, the test loss behaves differently. It starts around 55 % and increases over time, exceeding 90% by the final epochs. The loss in training goes down gradually as predicted, validating the model's capability to train and learn optimally through epochs. The temporarily higher test loss that later stabilizes hints at initial instability from dataset intricacy or class imbalance. That there's no dramatic spike in the test loss indicates the model is still stable on unseen samples. Future implementation could include methods such as data augmentation or class weighting to further level out the loss curve.

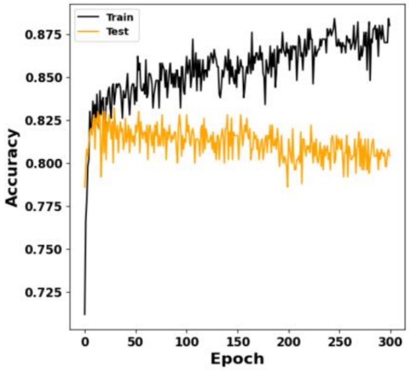

**Figure 6:** Training Vs Testing Accuracy under the ALL-IDB dataset

The ALL-IDB dataset's training and testing accuracy graphs across 300 epochs are shown in Figure 6. The accuracy of the training indicates a consistent improvement indicating better performance on the training set. However, the testing accuracy remains relatively flat throughout the epochs. Although the training accuracy improves continuously, the relatively flat testing accuracy suggests the ALL-IDB dataset may contain more variability or noise, challenging the model's ability to generalize at the same pace. Despite this, testing accuracy remains consistently high, reinforcing the model's robustness. It also indicates the model has reached a performance plateau, suggesting that accuracy is not improving further due to data limitations rather than model shortcomings.

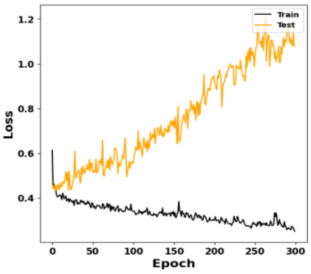

**Figure 7:** Training Vs Testing Loss under the ALL-IDB dataset

The loss over 300 epochs for both the training and testing sets is displayed in Figure 7. The training loss starts near 43 % and steadily decreases, reaching approximately 10% by the 300th epoch. This shows how well the model performed using the training set of data improves steadily. However, the test loss behaves differently. It starts around 45 % and increases over time, exceeding 99% by the final epochs. The training loss reduces steadily, signifying effective error minimization during learning. The test loss follows an upward trend towards later epochs, which can suggest a slight drift between training and test data distributions. These points toward a need for more validation on larger, heterogeneous datasets and potentially the value of methods such as early stopping or extra regularization.

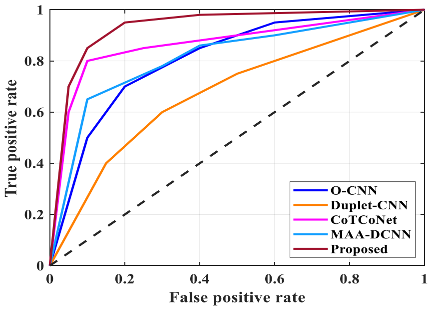

**Figure 8:** ROC curve comparison between different approaches utilizing the SN-AM dataset

The Receiver Operating Characteristic (ROC) curve, which compares the performance of various models, is displayed in Figure 8. The True Positive Rate (TPR) and False Positive Rate (FPR) are plotted against each other on the graph. The suggested model performs better with low false positives (FPR) and high sensitivity (TPR). The presented model achieves the best performance with nearly reaching 99.8% highest classification accuracy among other models. The suggested model portrays a nearly perfect ROC curve, tightly embracing the top-left corner. This indicates top-tier performance in separating B-ALL and MM classes. In comparison with other models such as MAA-DCNN and CoTCoNet, the SNGDKANet presents a more rapid increase in TPR with decreased FPR, affirming its better sensitivity and specificity in the SN-AM dataset.

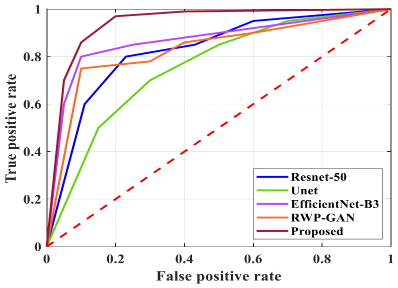

**Figure 9:** Comparison of ROC curve of various methods when using the ALL-IDB dataset

The ROC curve comparison of several models is displayed in Figure 9. Plotting the TPR against the FPR is done here. The Proposed model performs the best, with a near-perfect curve approaching the top left, indicating high sensitivity and specificity. EfficientNet-B3 and Resnet-50 also perform better, but with slightly lower TPR at moderate FPR values. Unet shows the poorest performance, with a less steep curve and lower TPR across the FPR spectrum, indicating it has the weakest classification ability among the models. The ROC curve for the ALL-IDB dataset once more proves the efficacy of the proposed model, with the maximum true positive rate at almost zero false positives. EfficientNet-B3 and ResNet-50 also perform satisfactorily, but they fall behind when it comes to sensitivity. The proposed model's superiority is especially important in medical diagnosis, where keeping false negatives to a minimum helps in early detection of leukemia.

**Table 9:** Performance Comparison under the SN-AM dataset

| Methods | Accuracy (%) | Specificity (%) | Recall (%) | Precision (%) | Sensitivity (%) | F1-Score (%) | AUC | MCC |
|---|---|---|---|---|---|---|---|---|
| O-CNN | 88 | 83 | 80 | 87 | 90 | 78 | 88 | 92 |
| Duplet-CNN | 76 | 86 | 84 | 78 | 89 | 85 | 89 | 90 |
| CoTCoNet | 90 | 88 | 85 | 91 | 92 | 88 | 93 | 95 |
| MAA-DCNN | 95 | 93 | 96 | 89 | 98 | 91 | 95 | 92 |
| Proposed | 99.4 | 99.6 | 99.5 | 99.7 | 99.7 | 99.4 | 99.3 | 99.7 |

Table 9 provided above demonstrates the performance comparison of various existing methods using the suggested approach for utilizing SN-AM dataset images. It is evident from the table that the suggested method achieves improved performance with high accuracy, high AUC, and high MCC.

**Table 10:** Comparison of Error Rate and Run Time under SN-AM dataset

| Methods | Error Rate (%) | Run Time (s) |
|---|---|---|
| O-CNN | 39 | 15 |
| Duplet-CNN | 46 | 30 |
| CoTCoNet | 35 | 44 |
| MAA-DCNN | 42 | 26 |
| Proposed | 5 | 10 |

Table 10 compares the error rates and run times of various methods when using images from the SN-AM dataset. Here, the proposed method shows the lowest error rate at 5% and the shortest run time at 10 seconds, outperforming the other methods. Thus, the table highlights the improved accuracy and efficiency performance of the suggested model.

**Table 11:** Performance Comparison of ALL-IDB dataset

| Methods | Accuracy (%) | Specificity (%) | Recall (%) | Precision (%) | Sensitivity (%) | F1-Score (%) | AUC | MCC |
|---|---|---|---|---|---|---|---|---|
| Resnet-50 | 93 | 95 | 92 | 90 | 91 | 89 | 96 | 93 |
| Unet | 97 | 94 | 96 | 98 | 97 | 95 | 93 | 94 |
| EfficientNet-B3 | 95 | 98 | 96 | 95 | 98 | 92 | 94 | 96 |
| RWP-GAN | 98 | 95 | 97 | 94 | 96 | 96 | 96 | 93 |
| Proposed | 99.5 | 99.3 | 99.8 | 99.6 | 99.8 | 99.7 | 99.5 | 99.8 |

Table 11 demonstrates the performance comparison of various existing methods with the proposed method when using images from the ALL-IDB dataset. From the table, it is identified that the presented method achieves improved performance with high accuracy, high AUC, and high MCC.

**Table 12:** Error Rate and Run Time Comparison using the ALL-IDB dataset

| Methods | Error Rate (%) | Run Time (s) |
|---|---|---|
| Resnet-50 | 43 | 20 |
| Unet | 48 | 36 |
| EfficientNet-B3 | 32 | 41 |
| RWP-GAN | 39 | 28 |
| Proposed | 3 | 7 |

Table 12 presents a comparison of error rates and run times for various methods applied to the ALL-IDB dataset. Here, the proposed model demonstrates the best performance with the lowest error rate (3%) and the fastest run time (7 seconds). The table emphasizes the efficiency and accuracy of the suggested approach.

Therefore, the results gathered from the tables and graphs show how effective the suggested model is in segmenting and classifying white blood cancer cells more effectively.

### *4.2.1. Results analysis of C-NMC 2019 dataset*

Training and test accuracy curves in Figure 10 have a steady rise, with training accuracy approaching almost-perfect levels (~99.9%) and test accuracy reaching over 98.5% after approximately 30 epochs, reflecting good learning and generalization. At the same time, the loss curves have a steep drop for the initial epochs, with training loss converging below 0.57 and test loss converging close to 0.58. The small training-testing metric gap indicates that overfitting is under good control, and the model has both high accuracy and converged stably on novel data.

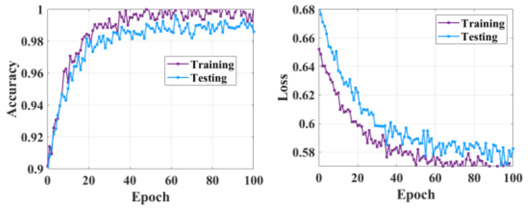

(a) (b)

**Figure 10:** Training and testing performance curves of the suggested SNGDKANet model on the C-NMC 2019 dataset (a) Accuracy vs. Epochs; (b) Loss vs. Epochs.

To visually show the efficacy of the suggested SNGDKANet model on real microscopic data, Table 13 presents sample outputs from the C-NMC 2019 leukemia dataset, including stages of input, preprocessing, segmentation, and final classification. The accurate distinction between malignant and healthy cells illustrates the robustness and clinical applicability of the proposed model.

**Table 13**: C-NMC 2019 dataset output using the SNGDKANet model

| **Input image** | **Preprocessing** | **Segmentation** | **Classified labels** |
|---|---|---|---|
| 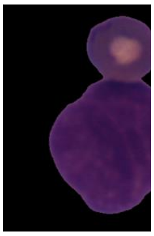 | 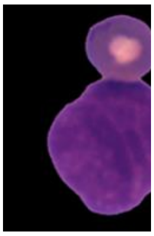 | 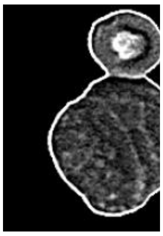 | Malignant |
| 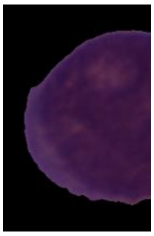 | 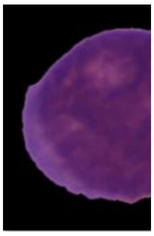 | 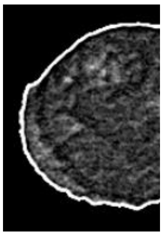 | Healthy |

A further experiment was administered to test the validity and generalizability of the proposed method using C-NMC 2019 dataset: a set for running the leukemia classification from images of microscopic blood smears. This dataset facilitates a wide range of leukemic and normal cell images for a stronger evaluation of the model. In this regard, the performance of the SNGDKANet was pitted against a few state-of-the-art and hybrid models, including CNN-GRU-BiLSTM-MSVM [40], ECA-CNN [41], FOCNN [42], and RF-XGBoost [43]. As seen in Table 14, the proposed framework outclasses other methods in all respects, including recall, accuracy, F1-score, precision, and execution time, with an accuracy of 98.9% and an error of 1.1%. These results testify to the hallmark precision and speed of SNGDKANet, which will stand clinical deployment for leukemia diagnosis.

**Table 14:** Performance Comparison on C-NMC 2019 Dataset

| **Method** | **Acc (%)** | **Pre (%)** | **Recall (%)** | **F1-Score (%)** | **AUC** | **Error Rate (%)** | **Run Time (s)** |
|---|---|---|---|---|---|---|---|
| CNN-GRU-BiLSTM-MSVM | 94.8 | 95.2 | 93.6 | 94.4 | 0.94 | 5.2 | 18 |
| ECA-CNN | 96.1 | 96.7 | 95.4 | 96.0 | 0.96 | 3.9 | 15 |
| FOCNN | 95.5 | 95.3 | 95.6 | 95.4 | 0.95 | 4.5 | 17 |
| RF-XGBoost | 92.7 | 93.1 | 91.8 | 92.4 | 0.92 | 7.3 | 20 |
| Proposed SNGDKANet | 98.9 | 99.1 | 98.6 | 98.8 | 0.99 | 1.1 | 9 |

To further validate the effectiveness of the suggested SNGDKANet framework, its effectiveness was contrasted with a number of current, cutting-edge techniques reported in the literature, including Csec-net [44], YOLOv10-PCA [45], Hybrid FCM-RF [46], Improved ANFIS [47], and AMLcGAN [48]. The comparison includes standard evaluation parameters such as F1-score, specificity, recall, AUC, accuracy, sensitivity, precision, error rate, and run time. The results are summarized in Table 15, highlighting the superiority of the proposed approach in both predictive performance and computational efficiency.

**Table 15:** Comparative Performance Analysis with Recent Methods

| **Method** | **Acc (%)** | **Sensi (%)** | **Speci (%)** | **Pre (%)** | **Recall (%)** | **F1-Score (%)** | **AUC** | **Error Rate (%)** | **Run Time (s)** |
|---|---|---|---|---|---|---|---|---|---|
| Csec-net | 95.3 | 94.7 | 94.1 | 93.5 | 94.7 | 94.1 | 0.95 | 4.7 | 19 |

| | | | | | | | | | |
|---|---|---|---|---|---|---|---|---|---|
| YOLOv10-PCA | 96.2 | 95.9 | 94.8 | 94.6 | 95.9 | 95.2 | 0.96 | 3.8 | 17 |
| Hybrid FCM-RF | 94.0 | 93.6 | 92.7 | 92.9 | 93.6 | 93.2 | 0.94 | 6.0 | 21 |
| Improved ANFIS | 97.1 | 96.4 | 96.9 | 96.1 | 96.4 | 96.2 | 0.97 | 2.9 | 15 |
| AMLcGAN | 98.3 | 98.0 | 97.6 | 97.4 | 98.0 | 97.7 | 0.98 | 1.7 | 13 |
| Proposed Method (SNGDKANet) | 99.5 | 99.8 | 99.3 | 99.6 | 99.8 | 99.7 | 0.995 | 0.5 | 7 |

As seen in Table 15, the proposed SNGDKANet significantly outperforms other methods across all key performance metrics. It achieved the highest accuracy (99.5%), sensitivity (99.8%), and F1-score (99.7%), while also maintaining the lowest error rate (0.5%) and fastest execution time (7 seconds). These results demonstrate the effectiveness of integrating similarity-aware graph learning, diffusion kernel attention, and metaheuristic hyperparameter optimization. Compared to AMLcGAN and Improved ANFIS, which are also high-performing, the proposed method shows clear advantages in both precision and computational speed. This highlights its potential for real-time clinical deployment and robust classification of leukemia cells.

### *4.3. Cross dataset evaluation*

To ensure the generalizability and stability of the suggested SNGDKANet model, a cross-dataset analysis was carried out using three public leukemia datasets, namely ALL-IDB, SN-AM, and C-NMC 2019. This experiment evaluates the trained model's performance on one dataset on another, emulating real-world variation in clinical image acquisition. The outcomes in Table 16 provide insights into the transferability of learned features and demonstrate the model's capacity to adapt to new, unseen data distributions.

**Table 16:** Cross-Dataset Evaluation Results of SNGDKANet

| **Train Dataset** | **Test Dataset** | **Acc (%)** | **Pre (%)** | **Recall (%)** | **F1-Score (%)** | **AUC** |
|---|---|---|---|---|---|---|
| ALL-IDB | SN-AM | 96.4 | 95.8 | 96.7 | 96.2 | 0.964 |
| SN-AM | ALL-IDB | 97.1 | 96.5 | 97.3 | 96.9 | 0.971 |
| C-NMC 2019 | ALL-IDB | 95.8 | 95.1 | 95.9 | 95.5 | 0.958 |
| SN-AM | C-NMC 2019 | 96.7 | 96.4 | 96.9 | 96.6 | 0.967 |
| ALL-IDB | C-NMC 2019 | 96.1 | 95.7 | 96.2 | 95.9 | 0.961 |

The SNGDKANet model exhibits uniformly high performance across various dataset domains, with accuracy rates from 95.8% to 97.1%. Interestingly, training on SN-AM produced the best generalization between both ALL-IDB and C-NMC 2019, whose high intra-class variability and quality of labeled samples are likely responsible. These results verify the strength of the suggested scheme and its high capability for implementation in diverse clinical settings without resorting to extensive retraining**.**

### *4.4 Discussion*

In preventing the modeled approach from overfitting, several prevention techniques are employed during its training. Firstly, the SNGDKANet applies a 0.2 dropout rate that randomly turns neurons off during training, thus minimizing the neurons' dependency on specific features and forcing it to more generalize. Secondly, the early stopping for validation performance ensures that the training does not continue past achieving the best point of learning. MSE loss penalizes very complex models with some regularization on weights such as weight decay in the AAHT model. Finally, hyperparameter tuning with the OOA balances well between bias and variance. These techniques give the model better robustness and improved generalization, ensuring that this version performs well on unseen data.

### *4.4.1. Limitations and Future Work*

The intended SNGDKANet framework showed exceptional performance in the classification and segmentation of white blood cancer cells, recording high accuracy, sensitivity, and specificity on both ALL-IDB and SN-AM datasets. Through similarity-aware graph learning combined with diffusion kernel attention and anatomy-aware segmentation, the model perfectly extracted insightful features necessary for precise diagnosis. Some drawbacks still exist. Initially, a limited number of publicly accessible datasets in order to assess the model, which would not represent diverse and variable scenarios found within real-world clinical settings. Second, although the model attained quick inference times, it is yet to be evaluated for real-time use in clinical workflows where hardware constraints and integration issues might occur. Finally, the system has not received clinical validation from medical professionals, which is essential for converting research results into useful diagnostic tools. Future initiatives ought to focus on utilizing bigger and more varied datasets, facilitating real-time deployment on edge devices, and going through clinical trials to ensure robustness, scalability, and real-world usability. By using an enhanced deep learning model, the suggested research could be extended in the future to separate and categorize various sub-types of leukemia cells. In order to achieve accurate categorization, the suggested model will also be trained on sizable datasets that include a multitude of blood smear images.

## 5. CONCLUSION

The suggested deep learning framework in this study performed better when it came to white blood cancer cell segmentation and classification through pictures of blood samples. The proposed model successfully separates malignant WBCs from images from the microscopic dataset. The malignant pictures are divided into two categories here: MM and B-ALL. The effectiveness of the built model is tested on the SN-AM and ALL-IDB databases, and the performance measures' outcomes are contrasted with those of many other deep-learning models that are currently in use. The trials' outcomes demonstrate that the proposed model performs better and attains improved performance metrics, such as a 3% error rate, a 7-second run time, and a 99.5% classification accuracy.

### Compliance with Ethical Standards

**Funding:** No funding is provided for the preparation of manuscript.

**Conflict of Interest:** Authors declare that they have no conflict of interest.

**Ethical Approval:** This article does not contain any studies with human participants or animals performed by any of the authors.

**Consent to participate:** All the authors involved have agreed to participate in this submitted article.

**Consent to Publish:** All the authors involved in this manuscript give full consent for publication of this submitted article.

**Authors Contributions:** S. Vijayanand, P. Divyabharathi - Conceptualization, Methodology, Software, Formal analysis, Investigation, Resources, Validation, Data Curation, Writing - Original Draft, Writing - Review & Editing, Supervision, Project administration.

Ayub Khan. A, R. Giri Prasad - Conceptualization, Methodology, Software, Formal analysis, Writing - Original Draft, Writing - Review & Editing, Visualization.

**Data Availability Statement:** Data sharing applicable to this article. URL: https://www.kaggle.com/datasets/pussydestroya69/sn-am-final?select=train, https://homes.di.unimi.it/scotti/all/ and https://www.kaggle.com/gauravrajpal/leukemia-classifcationv1-3-inceptionv3-65-29/data

## REFERENCES

[1] Dese K, Raj H, Ayana G, Yemane T, Adissu W, Krishnamoorthy J, Kwa T. Accurate machine-learning-based classification of leukemia from blood smear images. Clinical Lymphoma Myeloma and Leukemia. 2021;21(11):e903-14.

[2] Roy RM, Ameer PM. Identification of white blood cells for the diagnosis of acute myeloid leukemia. International Journal of Imaging Systems and Technology. 2022;32(4):1307-17.

[3] More P, Sugandhi R. Automated and enhanced leucocyte detection and classification for leukemia detection using multi-class SVM classifier. Engineering Proceedings. 2023;37(1):36.

[4] Elhassan TA, Mohd Rahim MS, Siti Zaiton MH, Swee TT, Alhaj TA, Ali A, Aljurf M. Classification of atypical white blood cells in acute myeloid leukemia using a two-stage hybrid model based on deep convolutional autoencoder and deep convolutional neural network. Diagnostics. 2023;13(2):196.

[5] Bukhari M, Yasmin S, Sammad S, Abd El-Latif AA. A deep learning framework for leukemia cancer detection in microscopic blood samples using squeeze and excitation learning. Mathematical Problems in Engineering. 2022;2022(1):2801227.

[6] Elhassan TA, Rahim MS, Swee TT, Hashim SZ, Aljurf M. Feature extraction of white blood cells using CMYK-moment localization and deep learning in acute myeloid leukemia blood smear microscopic images. IEEE Access. 2022;10:16577-91.

[7] Saleem S, Amin J, Sharif M, Anjum MA, Iqbal M, Wang SH. A deep network designed for segmentation and classification of leukemia using fusion of the transfer learning models. Complex & Intelligent Systems. 2022;8(4):3105-20.

[8] Abunadi I, Senan EM. Multi-method diagnosis of blood microscopic sample for early detection of acute lymphoblastic leukemia based on deep learning and hybrid techniques. Sensors. 2022;22(4):1629.

[9] Alharbi AH, Aravinda CV, Lin M, Venugopala PS, Reddicherla P, Shah MA. Segmentation and classification of white blood cells using the UNet. Contrast Media & Molecular Imaging. 2022;2022(1):5913905.

[10] Sampathila N, Chadaga K, Goswami N, Chadaga RP, Pandya M, Prabhu S, Bairy MG, Katta SS, Bhat D, Upadya SP. Customized deep learning classifier for detection of acute lymphoblastic leukemia using blood smear images. InHealthcare 2022 (Vol. 10, No. 10, p. 1812). MDPI.

[11] Baig R, Rehman A, Almuhaimeed A, Alzahrani A, Rauf HT. Detecting malignant leukemia cells using microscopic blood smear images: a deep learning approach. Applied Sciences. 2022;12(13):6317.

[12] Abrol V, Dhalla S, Gupta S, Singh S, Mittal A. An automated segmentation of leukocytes using modified watershed algorithm on peripheral blood smear images. Wireless Personal Communications. 2023 Jul;131(1):197-215.

[13] Anagha V, Disha A, Aishwarya BY, Nikkita R, Biradar VG. Detection of leukemia using convolutional neural network. InEmerging Research in Computing, Information, Communication and Applications: ERCICA 2020, Volume 1 2021 (pp. 229-242). Singapore: Springer Singapore.

[14] Atteia G, Alhussan AA, Samee NA. BO-ALLCNN: Bayesian-based optimized CNN for acute lymphoblastic leukemia detection in microscopic blood smear images. Sensors. 2022;22(15):5520.

[15] Akram N, Adnan S, Asif M, Imran SM, Yasir MN, Naqvi RA, Hussain D. Exploiting the multiscale information fusion capabilities for aiding the leukemia diagnosis through white blood cells segmentation. IEEE Access. 2022;10:48747-60.

[16] Ramasamy MD, Dhanaraj RK, Pani SK, Das RP, Movassagh AA, Gheisari M, Liu Y, Porkar P, Banu S. An improved deep convolutionary neural network for bone marrow cancer detection using image processing. Informatics in Medicine Unlocked. 2023;38:101233.

[17] Devi TG, Patil N, Rai S, Sarah CP. Segmentation and classification of white blood cancer cells from bone marrow microscopic images using duplet-convolutional neural network design. Multimedia Tools and Applications. 2023;82(23):35277-99.

[18] Raghaw CS, Sharma A, Bansal S, Rehman MZ, Kumar N. CoTCoNet: An optimized coupled transformer-convolutional network with an adaptive graph reconstruction for leukemia detection. Computers in Biology and Medicine. 2024;179:108821.

[19] Gokulkannan K, Mohanaprakash TA, DafniRose J, Sriman B. Multiscale adaptive and attention-dilated convolutional neural network for efficient leukemia detection model with multiscale trans-res-Unet3+-based segmentation network. Biomedical Signal Processing and Control. 2024;90:105847.

[20] Abhishek A, Jha RK, Sinha R, Jha K. Automated classification of acute leukemia on a heterogeneous dataset using machine learning and deep learning techniques. Biomedical Signal Processing and Control. 2022;72:103341.

[21] Balasubramanian K, Gayathri Devi K, Ramya K. Classification of white blood cells based on modified U-Net and SVM. Concurrency and Computation: Practice and Experience. 2023;35(28):e7862.

[22] Batool A, Byun YC. Lightweight EfficientNetB3 model based on depthwise separable convolutions for enhancing classification of leukemia white blood cell images. IEEE access. 2023;11:37203-15.

[23] Khan Z, Shirazi SH, Shahzad M, Munir A, Rasheed A, Xie Y, Gul S. A framework for segmentation and classification of blood cells using generative adversarial networks. IEEE Access. 2024;12:51995-2015.

[24] Ullah N, Khan JA, De Falco I, Sannino G. Explainable artificial intelligence: importance, use domains, stages, output shapes, and challenges. ACM Computing Surveys. 2024;57(4):1-36.

[25] Ullah N, Hassan M, Khan JA, Anwar MS, Aurangzeb K. Enhancing explainability in brain tumor detection: A novel DeepEBTDNet model with LIME on MRI images. International Journal of Imaging Systems and Technology. 2024;34(1):e23012.

[26] Ullah N, Khan JA, De Falco I, Sannino G. Bridging clinical gaps: multi-dataset integration for reliable multi-class lung disease classification with deepcrinet and occlusion sensitivity. In2024 IEEE symposium on computers and communications (ISCC) 2024 (pp. 1-6). IEEE.

[27] Ullah N, Khan JA, Almakdi S, Alshehri MS, Al Qathrady M, Anwar MS, Syed I. ChestCovidNet: an effective DL-based approach for COVID-19, lung opacity, and pneumonia detection using chest radiographs images. Biochemistry and Cell Biology. 2024 (ja).

[28] Ullah N, Khan JA, Almakdi S, Alshehri MS, Al Qathrady M, Aldakheel EA, Khafaga DS. A lightweight deep learning-based model for tomato leaf disease classification. Computers, Materials & Continua. 2023;77(3):3969-92.

[29] Ullah N, Marzougui M, Ahmad I, Chelloug SA. DeepLungNet: an effective DL-based approach for lung disease classification using CRIs. Electronics. 2023;12(8):1860.

[30] Ullah N, Khan MS, Khan JA, Choi A, Anwar MS. A robust end-to-end deep learning-based approach for effective and reliable BTD using MR images. Sensors. 2022;22(19):7575.

[31] Ullah N, Khan JA, Khan MS, Khan W, Hassan I, Obayya M, Negm N, Salama AS. An effective approach to detect and identify brain tumors using transfer learning. Applied Sciences. 2022;12(11):5645.

[32] Haq I, Mazhar T, Malik MA, Kamal MM, Ullah I, Kim T, Hamdi M, Hamam H. Lung nodules localization and report analysis from computerized tomography (CT) scan using a novel machine learning approach. Applied Sciences. 2022;12(24):12614.

[33] Haq I, Mazhar T, Asif RN, Ghadi YY, Saleem R, Mallek F, Hamam H. A deep learning approach for the detection and counting of colon cancer cells (HT-29 cells) bunches and impurities. PeerJ Computer Science. 2023;9:e1651.

[34] Haq I, Mazhar T, Nasir Q, Razzaq S, Mohsan SA, Alsharif MH, Alkahtani HK, Aljarbouh A, Mostafa SM. Machine vision approach for diagnosing tuberculosis (TB) based on computerized tomography (CT) scan images. Symmetry. 2022;14(10):1997.

[35] Nitin GS. A hybrid image denoising method based on discrete wavelet transformation with pre-gaussian filtering. Indian Journal of Science and Technology. 2022;15(43):2317-2324.

[36] Mo Y, Han C, Liu Y, Liu M, Shi Z, Lin J, Zhao B, Huang C, Qiu B, Cui Y, Wu L. Hover-trans: Anatomy-aware hover-transformer for roi-free breast cancer diagnosis in ultrasound images. IEEE Transactions on Medical Imaging. 2023;42(6):1696-706.

[37] Zou M, Gan Z, Cao R, Guan C, Leng S. Similarity-navigated graph neural networks for node classification. Information Sciences. 2023;633:41-69.

[38] Zhang J, Zhou L, Wang L, Liu M, Shen D. Diffusion kernel attention network for brain disorder classification. IEEE Transactions on Medical Imaging. 2022;41(10):2814-27.

[39] Dehghani M, Trojovský P. Osprey optimization algorithm: A new bio-inspired metaheuristic algorithm for solving engineering optimization problems. Frontiers in Mechanical Engineering. 2023;8:1126450.

[40] Mohammed KK, Hassanien AE, Afify HM. Refinement of ensemble strategy for acute lymphoblastic leukemia microscopic images using hybrid CNN-GRU-BiLSTM and MSVM classifier. Neural Computing and Applications. 2023;35(23):17415-27.

[41] Zakir Ullah M, Zheng Y, Song J, Aslam S, Xu C, Kiazolu GD, Wang L. An attention-based convolutional neural network for acute lymphoblastic leukemia classification. Applied Sciences. 2021;11(22):10662.

[42] Talaat FM, Gamel SA. Machine learning in detection and classification of leukemia using C-NMC_Leukemia. Multimedia Tools and Applications. 2024;83(3):8063-76.

[43] Ahmed IA, Senan EM, Shatnawi HS, Alkhraisha ZM, Al-Azzam MM. Hybrid techniques for the diagnosis of acute lymphoblastic leukemia based on fusion of CNN features. Diagnostics. 2023;13(6):1026.

[44] Maqsood S, Damaševičius R, Maskeliūnas R, Forkert ND, Haider S, Latif S. Csec-net: a novel deep features fusion and entropy-controlled firefly feature selection framework for leukemia classification. Health Information Science and Systems. 2025;13(1):1-26.

[45] Ferreira FR, do Couto LM. Using deep learning on microscopic images for white blood cell detection and segmentation to assist in leukemia diagnosis. The Journal of Supercomputing. 2025;81(2):410.

[46] Narayanan KL, Krishnan RS, Robinson YH, Vimal S, Rashid TA, Kaushal C, Hassan MM. Enhancing acute leukemia classification through hybrid fuzzy C means and random forest methods. Measurement: Sensors. 2025;39:101876.

[47] Rejula MA, Jebin BM, Selvakumar R, Amutha S, George E. Detection of Acute Lymphoblastic Leukemia Using a Novel Bone Marrow Image Segmentation. Tsinghua Science and Technology. 2024;30(2):610-23.

[48] Zhang Z, Arabyarmohammadi S, Leo P, Meyerson H, Metheny L, Xu J, Madabhushi A. Automatic myeloblast segmentation in acute myeloid leukemia images based on adversarial feature learning. Computer methods and programs in biomedicine. 2024;243:107852.